Geophysical Journal International

Geophys. J. Int. (2010) **180,** 1153–1169 doi: 10.1111/j.1365-246X.2009.04441.x

Rayleigh-wave phase-velocity maps and three-dimensional shear velocity structure of the western US from local non-plane surface wave tomography

F. F. Pollitz[1] and J. Arthur Snoke[2]

[1] *U.S. Geological Survey, Menlo Park,* CA 94025, *USA. E-mail: fpollitz@usgs.gov*
[2] *Virginia Polytechnic Institute and State University, Blacksburg,* VA 24061, *USA*

Accepted 2009 October 29. Received 2009 October 13; in original form 2009 June 26

SUMMARY

We utilize two-and-three-quarter years of vertical-component recordings made by the Transportable Array (TA) component of Earthscope to constrain three-dimensional (3-D) seismic shear wave velocity structure in the upper 200 km of the western United States. Single-taper spectral estimation is used to compile measurements of complex spectral amplitudes from 44 317 seismograms generated by 123 teleseismic events. In the first step employed to determine the Rayleigh-wave phase-velocity structure, we implement a new tomographic method, which is simpler and more robust than scattering-based methods (e.g. multi-plane surface wave tomography). The TA is effectively implemented as a large number of local arrays by defining a horizontal Gaussian smoothing distance that weights observations near a given target point. The complex spectral-amplitude measurements are interpreted with the spherical Helmholtz equation using local observations about a succession of target points, resulting in Rayleigh-wave phase-velocity maps at periods over the range of 18–125 s. The derived maps depend on the form of local fits to the Helmholtz equation, which generally involve the non-plane-wave solutions of Friederich et al. In a second step, the phase-velocity maps are used to derive 3-D shear velocity structure. The 3-D velocity images confirm details witnessed in prior body-wave and surface-wave studies and reveal new structures, including a deep ($>$100 km deep) high-velocity lineament, of width $\sim$200 km, stretching from the southern Great Valley to northern Utah that may be a relic of plate subduction or, alternatively, either a remnant of the Mojave Precambrian Province or a mantle downwelling. Mantle seismic velocity is highly correlated with heat flow, Holocene volcanism, elastic plate thickness and seismicity. This suggests that shallow mantle structure provides the heat source for associated magmatism, as well as thinning of the thermal lithosphere, leading to relatively high stress concentration. Our images also confirm the presence of high-velocity mantle at $\gtrsim$100 km depth beneath areas of suspected mantle delamination (southern Sierra Nevada; Grande Ronde uplift), low velocity mantle underlying active rift zones, and high velocity mantle associated with the subducting Juan de Fuca plate. Structure established during the Proterozoic appears to exert a lasting influence on subsequent volcanism and tectonism up to the Present.

Key words: Tomography; Surface waves and free oscillations; Seismic tomography; North America.

1 INTRODUCTION

The Transportable Array (TA) component of Earthscope's USArray (Fig. 1) by the end of this study period (mid 2008) covered all of western United States with an interstation spacing of about 70km. Only 3 years since its inception, the TA has already yielded significantly higher quality images than previously published of seismic structure of the western United States using body waves (e.g. Burdick *et al.* 2008; Roth *et al.* 2008; Sigloch *et al.* 2008) and surface waves (e.g. Yang & Ritzwoller 2008; Yang *et al.* 2008; Pollitz 2008).

These surface wave studies have used very similar approaches, all of which are closely related to the 'non-plane-wave' tomographic method developed by Friederich & Wielandt (1995). Assuming that a single mode branch (e.g. the fundamental mode) has been isolated, this method posits that observed surface wavefields may be

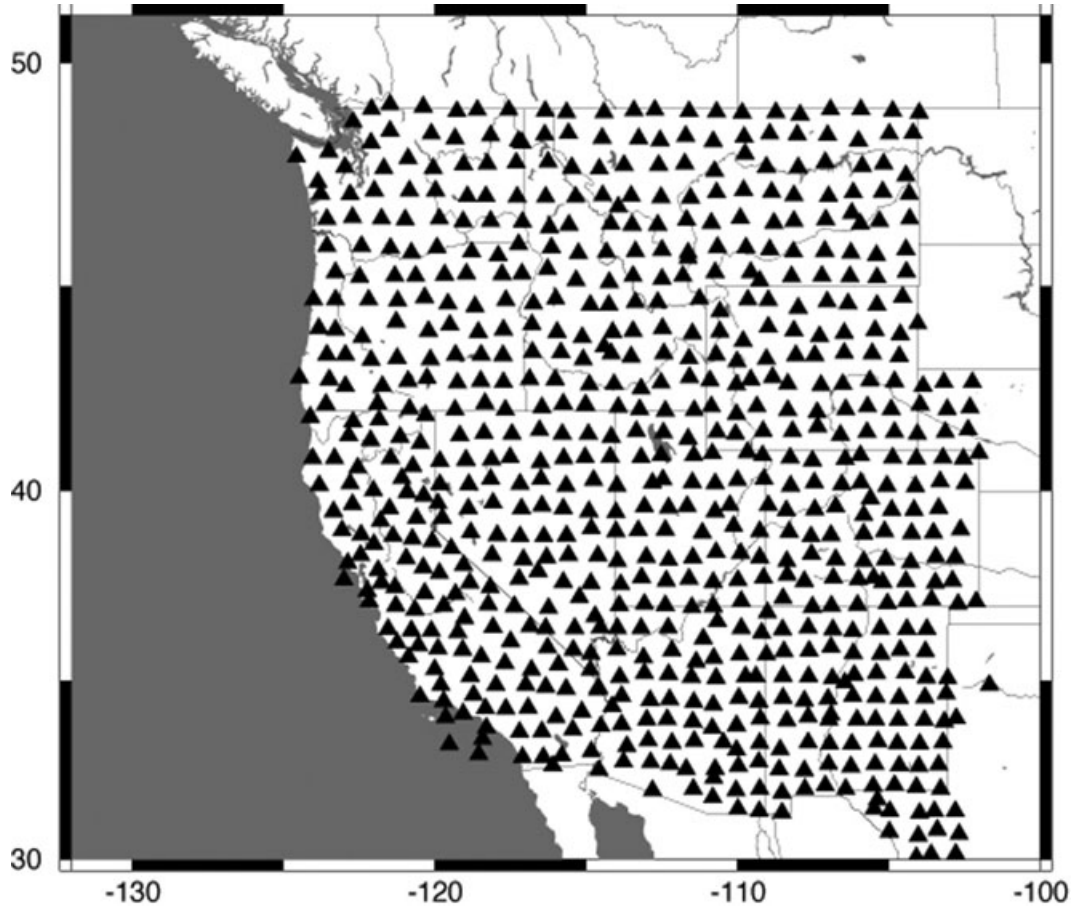

Figure 1. Distribution of broad-band stations of the TA used in this study.

represented as the sum of an 'incident' wavefield propagating on a laterally homogeneous reference structure plus a scattered wavefield produced by interaction of the full wavefield with laterally heteogeneous structure. Combinations of plane waves (more strictly, spherical waves on a spherical membrane) are used for the incident wavefields, and surface wave scattering theory (Snieder 1986; Romanowicz 1987; Pollitz 1999; Friederich 1999; Zhou *et al.* 2004) is used for the scattered wavefields. The implementations of this approach (Friederich 1998; Pollitz 1999, 2008; Yang *et al.* 2008) and the related 'two-plane wave' approach (Forsyth *et al.* 1998; Forsyth & Li 2005; Yang & Forsyth 2006; Yang & Ritzwoller 2008) indicate that there are considerable trade-offs between the roughness of the incident wavefields and the phase-velocity structure embodied in the scattered wavefields. Theoretically, all observed surface waves could be modelled as a superposition of a large number of plane waves propagating on a laterally homogeneous structure (Wielandt 1993; Friederich & Wielandt 1995), and the level of admissible laterally heterogeneous structure thus depends considerably on the parameterization of the incident wavefields.

The purpose of this study is to update the data set of Pollitz (2008) to include data collected since October, 2007—more than doubling the number of observations and increasing the frequency range, to revise the method of data analysis and to implement a more direct and simpler method for determining seismic surface-wave phase-velocity distributions. These methods are applied to a large data set of fundamental-mode Rayleigh wave spectra observed by the TA.

2 DATA SET

We use 44,317 vertical-component seismograms from 123 teleseismic events of magnitude $\geq$6.3 which occurred from April 2006 to January 2009. The portions of the seismograms corresponding to a group velocity window from 2.9 to 4.3 km s^{-1} are isolated, and complex spectral amplitudes measured using a single taper method described later. Spectrograms are used to identify the Rayleigh wave dispersion and determine the frequency-dependent group velocity at which complex spectral amplitudes are estimated.

Let $U(f)$ be frequency-dependent group velocity averaged over the teleseismic propagation path. A single taper spectral estimation (Warren *et al.* 2008) is used to obtain Rayleigh wave dispersion. Examples of the spectrograms are shown in Fig. 2. These were determined by application of a suitable taper $w(t)$ to each record, determination of frequency-dependent group arrival time $t_{\rm group}(\omega) = \Delta/U(f)$, where Δ is epicentral distance, and estimation of the complex spectral amplitudes for vertical displacement. If the taper is highly bandlimited, then at angular frequency $\omega = 2\pi f$ this is given by (e.g. Pollitz 1999)

$$u(\omega) = \frac{1}{R(\omega)} \frac{F[u(t)w(t)](\omega)}{w(t_{\rm group})} \tag{1}$$

where $u(t)$ is the observed seismogram,

$$F[x(t)](\omega) = \int_0^\infty x(t) \exp(-i\omega t)\, dt \tag{2}$$

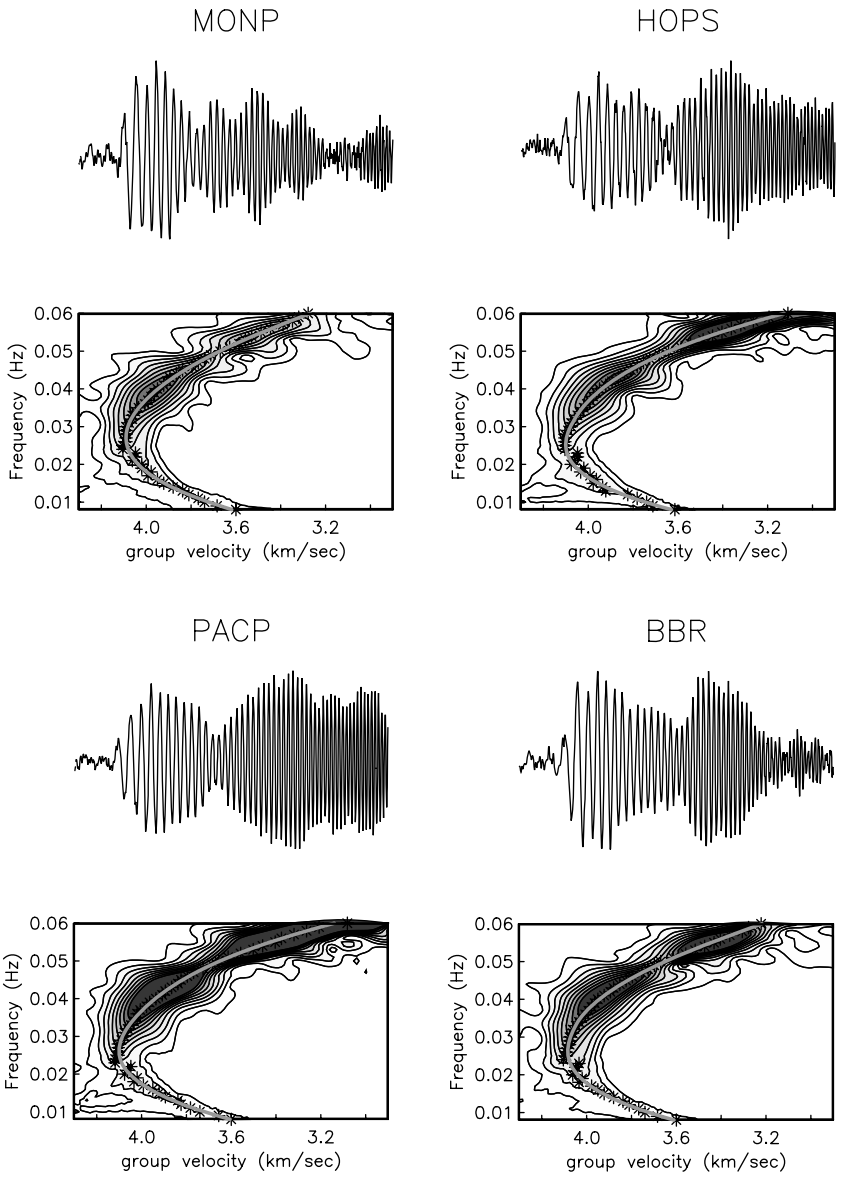

Figure 2. Vertical-component seismograms and associated spectrograms from seven TA receivers (inset) which recorded the 31 January 2007 event of magnitude 6.5 in the southwest Pacific (event #3 in Pollitz 2008). For a given spectrogram, symbols * indicate the group velocity $U(f)$ at which spectral amplitude at frequency f is maximum, and the superimposed grey curves are a cubic-spline fit to $U(f)$ with a break point at fixed frequency 0.034 Hz.

is the Fourier transform and $R(\omega)$ denotes instrument response.

The choice of taper is based on consideration of resolution in frequency f versus resolution in time or, equivalently, group velocity U. Sufficient resolution in both are needed to isolate the fundamental mode and determine group arrival times accurately. For symmetric tapers centered on the group arrival time, Wielandt & Schenk (1983) show that the bias in measured spectral amplitude and phase is related to the several quantities: the slope of the group delay versus f curve, the slope and curvature of the amplitude versus f curve, the position of the center of the time window, and the width of the taper, which controls the amount of spectral leakage. We find that spectral leakage is a potentially serious at $f \gtrsim 0.04$ Hz, where the slope of the U versus f curve is generally steep, and resolution in time is important at $f < 0.015$ Hz to avoid contamination with higher mode energy. A single taper constructed from a collection of Slepian eigentapers may be used for this purpose (Park *et al.* 1987; Pollitz 1999, 2008). However, it is not straightforward to control the resolution in time of such a taper, for example the example taper shown in Fig. 3 of Pollitz (2008), which has considerable temporal sidelobes. Here we employ a symmetric taper centered at the group arrival time, choosing the Hann taper for this purpose. The taper is tailored for the frequency being measured and is of the form

$$w(t)|_f = \begin{cases} \cos\left[\frac{1}{2}\frac{(t-t_{\rm group})}{T'}\frac{\pi}{2}\right] & (|t-t_{\rm group}| < 2T' \\ = 0 & (|t-t_{\rm group}| \geq 2T' \end{cases} \tag{3}$$

where

$$T' = \begin{cases} \left(\frac{\Delta}{\Delta_0}\right)^{1/2}\frac{1}{f} & (f < f_0) \\ \left(\frac{\Delta}{\Delta_0}\right)^{1/2}\frac{1}{f}\left[\frac{f}{f_0}\right]^{\gamma} & (f \geq f_0) \end{cases} \tag{4}$$

Here Δ_0 and f_0 are a reference epicentral distance and reference frequency, respectively. The factor $\sqrt{(\Delta/\Delta_0)}$ follows from eq. (13) of Wielandt & Schenk (1983), which dictates that the window width

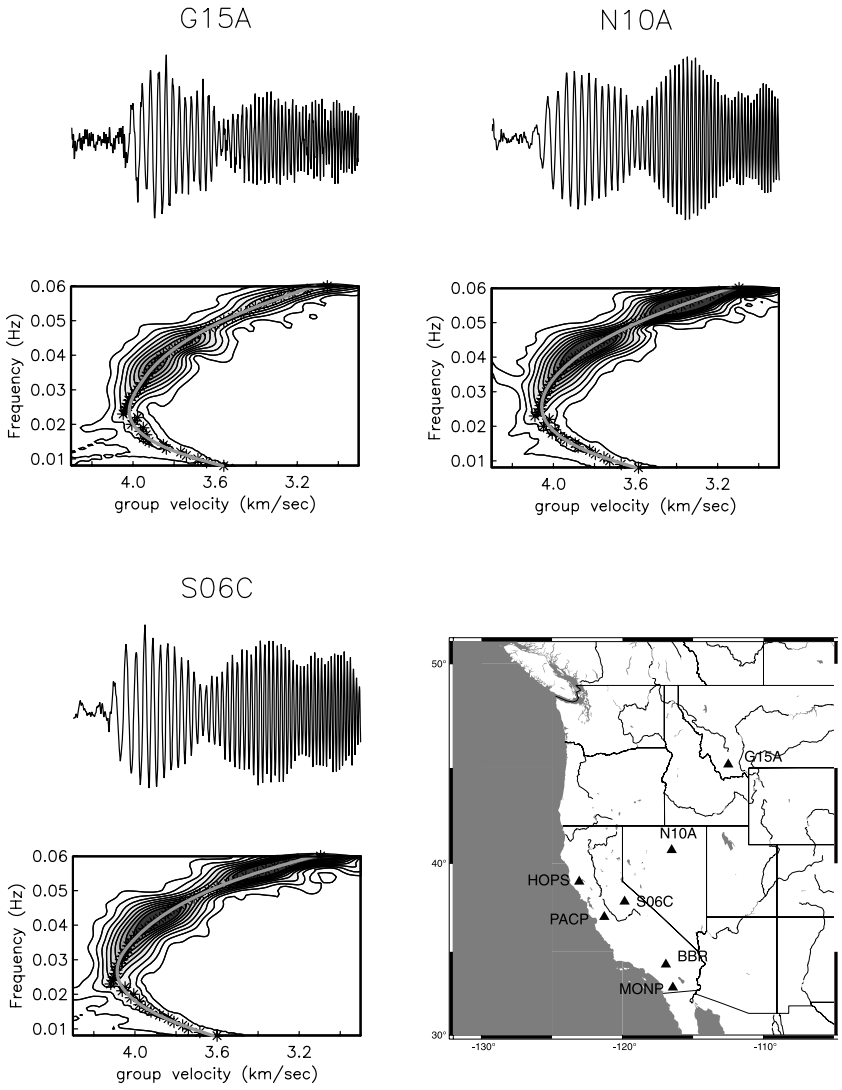

Figure 2. (*Continued*.)

should be proportional to the square root of the group delay time, which is proportional to Δ. Because group delay time equals Δ/U, Wielandt and Schenk's eq. (13) further indicates that T' should vary with frequency as $\sqrt{|dU(f)/df|}$ when this quantity is large. The factor $(f/f_0)^\gamma$ with constant γ is meant to mimick this frequency dependence, that is to capture the broadness of group arrivals at relatively high f where $U(f)$ generally decreases rapidly with f.

We find that $\Delta_0 = 90^\circ$, $f_0 = 0.025$ Hz, and $\gamma = 2$ are practical choices that yield reasonable resolution in both frequency and group velocity. At the reference distance $\Delta = \Delta_0$, the half-width of the taper is two periods at period $\geq$40 s, and the half-width is $80(f/f_0)^{\gamma-1}$s at all periods $<$40 s. This taper accommodates the desired resolution in time (or group velocity) at relatively long period and resolution in frequency at relatively short period. The ratio of taper width to period increases as f^γ for $f > f_0$, which may be helpful for capturing a wider range of scattered group arrivals expected at higher frequency.

The spectrograms calculated according to the earlier prescription have been checked against those calculated with the FTAN algorithm (e.g. Dziewonski *et al.* 1969; Levshin *et al.* 1989; Nyman & Landisman 1977), which employs narrow-band Gaussian filters. For both synthetic and actual data, the two algorithms agree with one another very closely.

Figs 4 and 5 show examples of application of this procedure to synthetic seismograms from two events at epicentral distances of 85.5° and 52.5°, respectively. It establishes that the Rayleigh wave dispersion is reasonably accurately estimated—and the frequency-dependent amplitude and phase are estimated with little bias-using $\gamma = 2$. Phase bias of up to 0.3 radians amounts to several parts in 10^4 error in average wavenumber along the teleseismic propagation path. If such errors without correlation existed at two closely spaced stations, the resultant error in estimated wavenumber between the stations would be much larger. However, it is expected that the systematic bias should be similar at closely located sites where the factors contributing to the bias are similar (e.g. those summarized in eq. 11 of Wielandt & Schenk 1983). Small jumps in the phase response are due to imperfect centering of the window, arising from an estimated group velocity that differs from the theoretical group velocity. A phase error arises from any imperfect centering (eq. 14 of Wielandt & Schenk 1983), and the jumps arise because group velocity is quantized in units of 0.007 km s^{-1} in these examples.

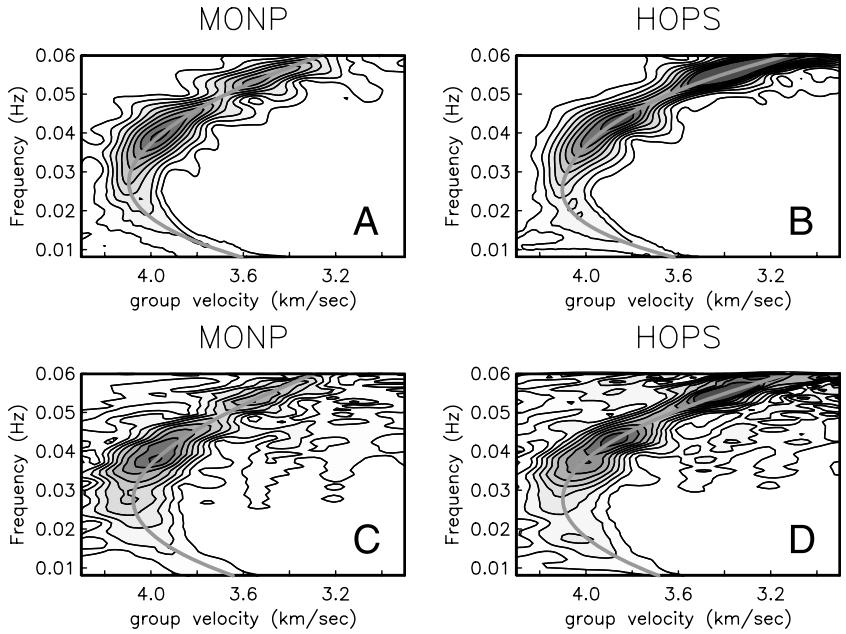

Figure 3. Spectrograms at MONP and HOPS from their recordings of the 2007 January 31 event. Different spectrograms result from use of a single taper prescribed by either the Hann taper (A and B) (this method) or constructed with a linear combination of eigentapers (C and D) (Pollitz 2008). The superimposed grey curves are as in Fig. 2.

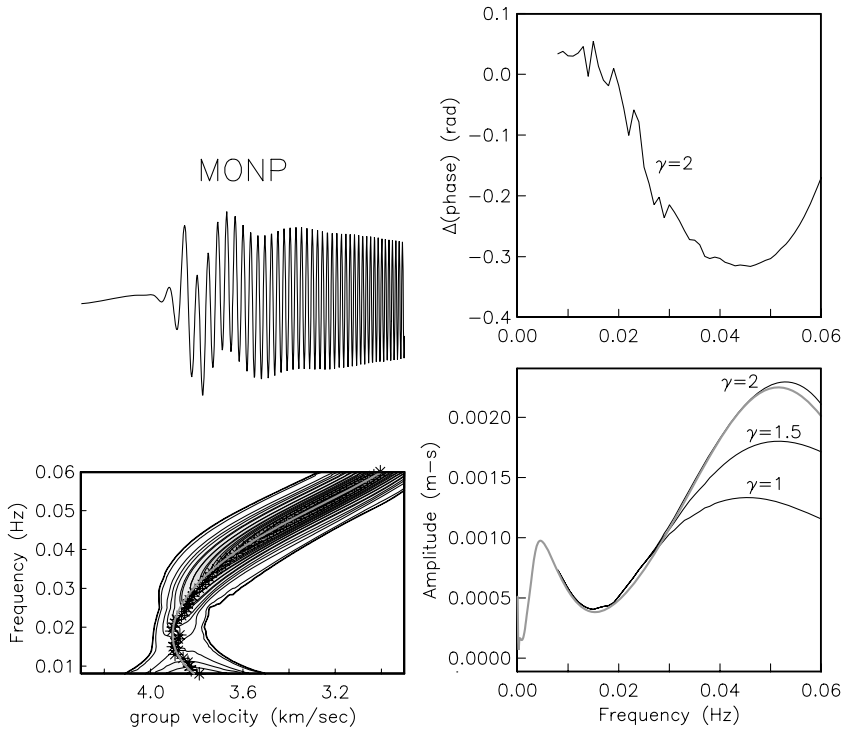

Figure 4. (Left) Synthetic vertical-component seismogram and associated spectrogram at MONP on the PREM model (Dziewonski & Anderson 1981) for a M6.5 event on 2007 January 31 (the event discussed in Fig. 2). The epicentral distance to MONP is 85.5°. Symbols * indicate the group velocity $U(f)$ at which spectral amplitude at frequency f is maximum, and the superimposed grey curve is the theoretical group velocity. $\gamma = 2$ has been used when employing eq. (4). (Right) Frequency-dependent spectral amplitude of $u(\omega)$ (eq. 1) estimated on the synthetic seismogram, and the difference between the phase of $u(\omega)$ using $\gamma = 2$ and the theoretical phase. Amplitude curves are shown for various values of γ, and the grey curve indicates the theoretical amplitude.

Using trial values of U from 2.9 to 4.3 km s^{-1}, $u(\omega)$ of the fundamental mode is taken at that group velocity $U = \hat{U}(f)$ for which $|u(\omega)|$ is maximized ("*" symbols in the figures). A smooth polynomial fit to the dispersion curve $\bar{U}(f)$ is fit to the set of $\hat{U}(f)$ (curves in Fig. 2). Variations expected for first-arriving fundamental modes are well captured with a piecewise cubic spline fit (Lawson & Hanson 1974) of the observed dispersion with a break point at 0.034Hz. For a given event, a 'summary' group velocity curve is

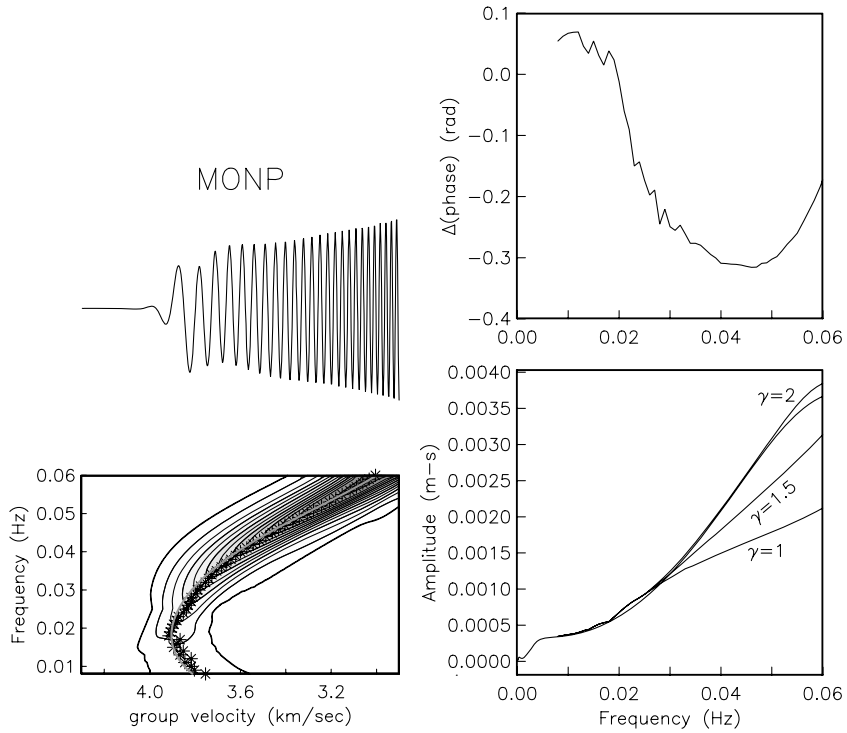

Figure 5. (Left) Synthetic vertical-component seismogram and associated spectrogram at MONP on the PREM model for a M6.4 event on 2007 February 24. The epicentral distance to MONP is 52.5°. See Fig. 4 for additional explanation.

defined as the average of the $\bar{U}(f)$ curves obtained for individual recordings of that event.

The use of the Hann taper generally yields simpler spectrograms than those produced by the eigentaper method of Pollitz (2008). The single taper used in the latter method is a linear combination of Slepian eigentapers and, at a target group arrival time, invariably has temporal sidelobes with secondary local maxima typically hundreds of seconds removed from the target group arrival time. Comparison of spectrograms produced by the two methods (Fig. 3) reveals artefacts in spectral amplitude using the eigentaper method. These appear as sidelobes around the main dispersion curve and result from the sampling of the dominant group energy by temporal sidelobes of the taper. Although the single taper constructed from the eigentapers carries the advantage of less spectral leakage than the employed Hann taper, we prefer to use the Hann taper in our analysis because of its better resolution in time and hence group velocity.

The measurements of displacement spectra furnish estimates of the Rayleigh wave potential $\tilde{\Phi}$, which is proportional to $u(\omega)$. Following Pollitz (1999), quality criteria are applied to edit the set $\{\tilde{\Phi}(\omega; \mathbf{r}_i)\}$ for a collection of receivers $\{\mathbf{r}_i\}$. For a given seismogram and target frequency, these are based on the consistency of the record's $\hat{U}(f)$ with the event's summary group velocity curve, as well as the variance of the record's $\hat{U}(f) - \bar{U}(f)$ within a range of f about the target frequency. These criteria are designed to check that the same seismic phase is consistently identified from record to record and that the fundamental mode Rayleigh wave is of sufficiently high amplitude (e.g. above the noise level) and isolated from higher modes. At a given frequency, sources for which less than 60 percent of available measurements are retained are eliminated. As a result of applying the quality criteria, the set of acceptable sources varies according to frequency (Fig. 6), and the set of seismic stations that yield acceptable observations varies according to the source and frequency.

3 DETERMINATION OF PHASE-VELOCITY DISTRIBUTION

On a laterally homogenous structure, the surface wavefield of an isolated mode branch satisfies a spherical Helmholtz equation with a constant phase velocity (e.g. Tromp & Dahlen 1993). In a $r-\theta-\phi$ spherical coordinate system, using $\mathbf{r}$ to represent colatitude θ and longitude ϕ, at fixed angular frequency ω this equation is

$$c^2\nabla^2\Phi + \omega^2\Phi = 0 \tag{5}$$

where ∇ is the surface gradient operator, $c(\omega)$ is a laterally homogeneous phase velocity and $\Phi(\omega; \mathbf{r})$ is the Rayleigh wave potential. For a single mode branch (assumed here to be the fundamental mode branch), Φ equals the spectrum of the vertical velocity multiplied by the vertical eigenfunction. For a single mode branch, eq. (5) is also valid for a laterally heterogeneous phase-velocity distribution $c(\omega, \mathbf{r})$ provided that it is characterized by smooth lateral perturbations (Tromp & Dahlen 1993; Friederich *et al.* 2000). For rougher lateral perturbations, eq. (5) with laterally heterogeneous c is also valid for surface wave propagation through an acoustic medium (Wielandt 1993), which involves only isotropic scattering interactions. The isotropic scattering approximation is valid if the azimuthal distribution of sources about the study area is sufficiently diverse to average out non-isotropic scattering interactions (e.g. Alsina *et al.* 1996; Friederich 1998).

Numerical experiments by Friederich *et al.* (2000) suggest that the spherical Helmholtz equation with laterally heterogeneous phase velocity is valid under the more liberal condition that the receiver network be dense enough to account for non-plane-wave effects

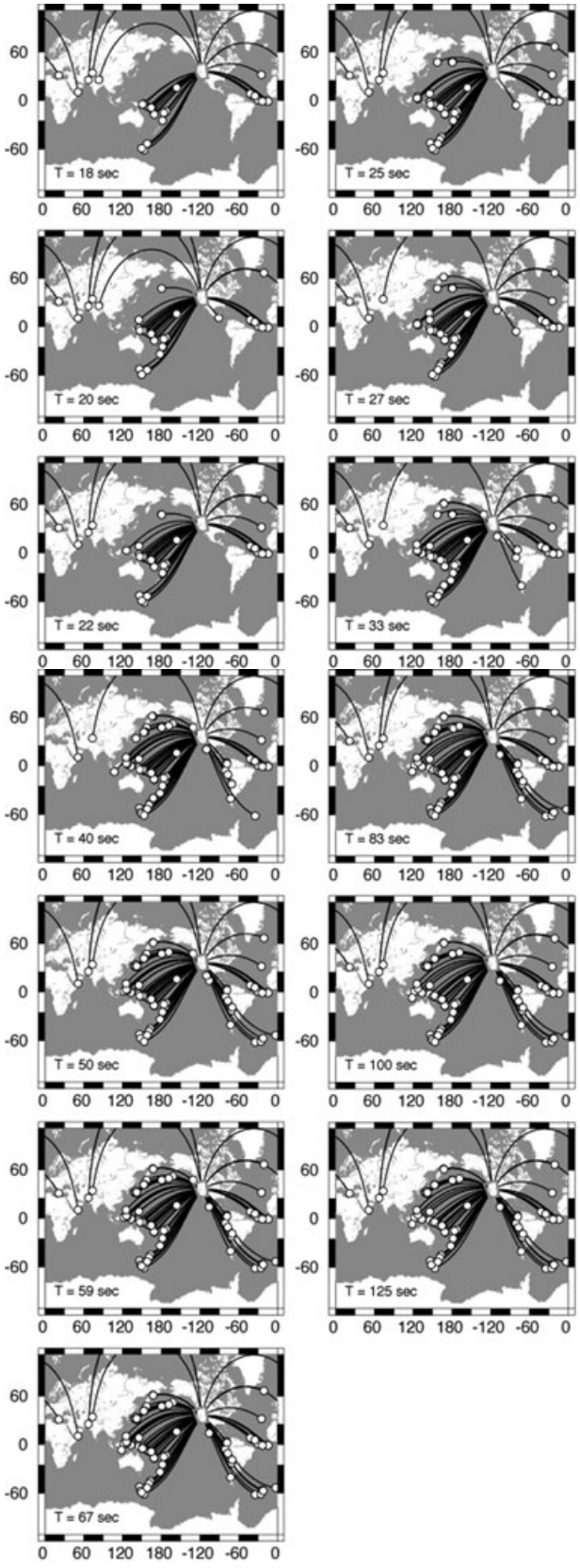

Figure 6. Distribution of teleseismic sources used in the inversion for phase-velocity structure, as a function of period. The distributions vary from period to period because of selection criteria applied to the frequency-dependent measurements of complex spectral amplitudes (Pollitz 1999). Superimposed are the minor arc paths to the TA.

(i.e. interference among several plane waves propagating with the same phase velocity Wielandt 1993). In this situation, the network samples the surface wavefield sufficiently to resolve lateral amplitude variations and hence their contribution to 'dynamic' phase velocity, thereby permitting the retrieval of structural phase velocity.

The validity of the spherical Helmholtz equation can be justified from scattering theory if applied to a relatively small area of dimension of roughly one wavelength or less. Within this area, scattering effects from local structure are implicity accounted for by solving eq. (5) with laterally homogeneous c representative of the area, and scattering from structure external to this area generally produces complicated incident wavefields (composed of numerous interfering plane waves) which nonetheless propagate in the target area according to eq. (5). To make these statements more precise, we assume that a target point $\mathbf{r}_0$ is surrounded by a small area A that contains a number of receivers, and let the reference Earth structure and actual Earth structure be denoted by $\mathbf{m}_0$ and $\mathbf{m}$, respectively. For a target mode branch α, surface wave scattering theory relates the Rayleigh wave potential to a spherical Earth structure via an integral equation of the form (Snieder 1986; Romanowicz 1987; Pollitz 1999; Friederich 1999; Zhou *et al.* 2004)

$$\Phi^{\alpha}(\mathbf{r}) = \Phi_0^{\alpha}(\mathbf{r}, \mathbf{r}') + \int \sum_{\alpha'} K^{\alpha\alpha'}(\mathbf{r}, \mathbf{r}')\Phi^{\alpha'}(\mathbf{r}')\, G(\mathbf{r}, \mathbf{r}'; k_0)\, d^2\mathbf{r}' \quad (6)$$

where Φ_0^{α} is the potential on $\mathbf{m}_0$, k_0 is the wavenumber of mode branch α on $\mathbf{m}_0$, the $K^{\alpha\alpha'}$ are differential operators which prescribe how an incident wavefield $\Phi^{\alpha'}$ interacts with a spherical structure $\mathbf{m} - \mathbf{m}_0$ to produce a scattered wavefield on mode branch α, and G satisfies

$$\nabla^2 G + k_0^2 G = \delta(\mathbf{r}, \mathbf{r}') \quad (7)$$

where $\delta(\mathbf{r}, \mathbf{r}')$ is the Dirac δ-function on a spherical membrane. The integral in eq. (6) may be split into two parts:

$$\Phi^{\alpha}(\mathbf{r}) = \Phi_0^{\alpha}(\mathbf{r}, \mathbf{r}') + \left[\int_{\mathbf{r}'\in A} + \int_{\mathbf{r}'\notin A}\right] \times \sum_{\alpha'} K^{\alpha\alpha'}(\mathbf{r}, \mathbf{r}')\Phi^{\alpha'}(\mathbf{r}')G(\mathbf{r}, \mathbf{r}'; k_0)\, d^2\mathbf{r}'. \quad (8)$$

If A is sufficiently small and $\mathbf{m}_0$ is the laterally averaged structure over A, then the first integral is relatively small. For $\mathbf{r} \in A$, the second integral (including all converted higher modes in the α'-summation) satisfies eq. (5) with constant $c = \omega/k_0$, as does the leading term Φ_0^{α}. Thus eq. (5) forms the basis for estimating the constant phase velocity $c(\omega)$ in the vicinity of a target point $\mathbf{r}_0$, which may be interpreted as the local phase velocity (e.g. Romanowicz 1987) and related to radial integrals of the local 3-D seismic structure. The contributions of the first integral in eq. (8) as well as arriving higher mode energy are considered sources of noise that diminish in importance with an increasing number of observations. This approach, here termed 'local non-plane surface-wave tomography', essentially takes advantage of the aperture and density of the TA to constrain local phase velocity.

In detail, this method is applied to observations of Rayleigh wave potential $\tilde{\Phi}^{(n)}(\omega, \mathbf{r}_i)$ for a collection of seismic sources with index n and a set of receivers with index i. For a target point $\mathbf{r}_0$ we construct a solution to eq. (5) using the squared misfit of $\Phi^{(n)}$ to $\tilde{\Phi}^{(n)}$ weighted by a Gaussian exponential which effectively restricts consideration to observations at only those receivers $\mathbf{r}_i$ within a limited distance

from $\mathbf{r}_0$. We minimize a function of the form

$$\chi^2(\mathbf{r}_0; c(\omega)) = \sum_{n=1}^{N} \sum_{i \in \text{Event}\#n} \left| \tilde{\Phi}^{(n)}(\omega, \mathbf{r}_i) - \Phi^{(n)}(\omega, \mathbf{r}_i; c(\omega)) \right|^2 \times \exp\left(-\frac{1}{2} \frac{|\mathbf{r}_0 - \mathbf{r}_i|^2}{d^2} \right) \quad (9)$$

where the argument $c(\omega)$ is added to the model function $\mathbf{\Phi}^{(n)}$ to emphasize that it satisfies eq. (5) with that phase velocity; d is a Gaussian smoothing distance.

Admissible forms of Φ are any superposition of plane waves propagating with constant wavenumber $k = \omega/c(\omega)$, for example the waves W_l given in eq. (9) of Pollitz (2008) and shown in supplementary fig. S3 of (Pollitz 2008). A practical form of Φ is the truncated expansion

$$\Phi^{(n)}(\omega, \mathbf{r}; c(\omega)) \equiv a_{-1}^{(n)} W_{-1}(\omega, \mathbf{r}; c(\omega)) + \sum_{l=0}^{l_{\max}} a_l^{(n)} W_l(\omega, \mathbf{r}; c(\omega))$$

$$W_{-1} = Q^{(1)}_{(k-1/2)0}(\cos\theta)$$

$$W_l = \int \left\{ h_l(\mu L) \exp\left[-\frac{(\mu L)^2}{2} \right] \right\} \left[Q^{(1)}_{(k-1/2)\mu}(\cos\theta) \exp(i\mu\phi) \right] (-k)^{-\mu} \exp\left(i\mu \frac{\pi}{2} \right) d\mu \quad (10)$$

where the $Q^{(1)}_{(k-1/2)\mu}(\cos\theta)\exp(i\mu\phi)$ are travelling-wave Legendre functions (Appendix B of Dahlen & Tromp (1998)) with θ and ϕ denoting the source–receiver distance and azimuth, h_l is a Hermite polynomial of degree l (Abramowitz & Stegun 1972), L is a scale factor and the a_l are complex constants. This is eq. (9) of Pollitz (2008) with the additions of the source index n and $c(\omega)$ in the arguments of the wavefields. The W_{-1} term represents (the spherical equivalent of) a single plane wave arriving directly from the source backazimuth. Each higher W_l term represents a superposition of plane waves arriving from a continuum of source backazimuths (with backazimuth equal to $\sin^{-1}(\mu/K_0)$), with a weighting function that is a smoothly varying function of backazimuth.

With this parameterization of $\Phi^{(n)}$, $c(\omega)$ at the target point $\mathbf{r}_0$ is determined in two steps. First, $\chi^2(\mathbf{r}_0; c(\omega))$ is minimized by solving N systems of simultaneous equations, one system for each source consisting of either $L = 1$ or $L = l_{\max} + 2$ equations, depending on whether the second summation of eq. (10) is included in the expansion of $\Phi^{(n)}$:

$$\frac{\partial \chi^2}{\partial a_l^{(n)}} = 0 \qquad (l = -1, 0, \ldots, L-2). \quad (11)$$

Second, a grid search in $c(\omega)$ is performed to identify that c for which χ^2 achieves a global minimum. This procedure is repeated at a dense set of target points $\mathbf{r}_0$ within the TA network.

The choice of Gaussian smoothing distance d to be used in eq. (9) depends chiefly on two considerations—the interstation distance and the wavelength at a given period. A typical interstation distance is 70km, and wavelength λ increases as a function of period from about 63 km at 18 s to 500km at 125 s period. A value $d = 50$km for period ≤ 50s and gradually increasing d at longer period yields reasonable results. For a given epicentral distance, the horizontal scale of the Fresnel zones and associated sensitivity kernels varies with wavelength as $\sim \sqrt{\lambda}$ (Wang & Dahlen 1995; Nolet & Dahlen 2000). With sufficient sampling of the wavefield around the target point, observations of the surface wavefield will sample roughly the same average structure as a function of period provided that the Gaussian smoothing parameter varies as $\sqrt{\lambda}$. From these considerations, we choose

$$d = \begin{cases} 50\,\text{km} & T \leq 50\,\text{sec} \\ 50\sqrt{\frac{\lambda}{\lambda_0}}\,\text{km} & T > 50\,\text{sec} \end{cases} \quad (12)$$

where λ_0 is the wavelength at $T = 50$ s.

We find that $l_{\max} = 1$ in eq. (10), consisting of one plane wave term (the W_{-1} term) and two non-plane-wave terms (the W_0 and W_1 terms), is sufficient to capture incident wave complexity within the vicinity of a typical target point and that there is sufficient sampling of the wavefield at any target point to estimate the 6 parameters which define $\Phi^{(n)}$ for a given event. There are usually five to six TA stations within 120 km of a target point, each of which contributes a complex spectral amplitude measurement with a significant weight, hence effectively 10–12 observations.

This approach to estimating phase velocity involves fitting a spatial function (i.e. eq. 10) to the frequency-transformed seismic signal. This differs from the method of Cara (1978), which involves calculating an array response function using a joint frequency and spatial transform. The two approaches will closely agree if the locally incident signal behaves as a plane wave for each frequency component. The fitting method used in our study permits a natural extension to the case of locally incident non-plane waves. Both methods permit the estimation of phase-velocity variations across the array.

To the extent that general solutions of eq. (5) involve curved wavefronts, the solutions given by eq. (10) are closely related to the eikonal tomography (e.g. Lin *et al.* 2009) method. The solutions given by eq. (10) contain both phase and amplitude information, both of which are used in fitting complex amplitude spectra for optimal local phase velocity. Because the phase front could be extracted from these solutions and used as the basic observable, this method embraces the eikonal tomography approach, which exploits only phase information. (Although Lin *et al.* (2009) ignore lateral gradients of surface-wave amplitude, they note that such gradients could, in principle, be incorporated into the estimation of local phase-velocity structure via their eq. (2).) A significant advantage of the eikonal tomography approach is its direct mapping of wavefronts into phase-velocity structure and its adaptability to inferring azimuthally anisotropic structure. We note that our method is also adaptable to the case of azimuthal anisotropy, where local phase velocity would further depend upon the azimuth of the wave propagation direction (Smith & Dahlen 1973). This could be incorporated into the definition of the basis functions used to define the non-plane wave solutions of eq. (9) of Pollitz (2008), which would yield a dependence of the wavefield potentials of eq. (10) on the local values of the parameters that describe this azimuth dependence. The procedure for estimating local $c(\omega)$ would then be modified to estimate the additional local anisotropic parameters.

4 RESULTS

The resulting phase-velocity maps are shown in Fig. 7. At the shortest periods the maps have gaps because phase velocity was judged indeterminate wherever a global minimum in χ^2 was not achieved within pre-set bounds for $c(\omega)$. This is seen mostly in the eastern part of the TA which has been operating for a shorter time.

The standard error in estimated phase velocity may be estimated as follows. For source #n, let the angular distance to and $\mathbf{r}_0$ and $\mathbf{r}_j$ be Δ and $\Delta_j^{(n)}$, respectively. In the plane wave approximation, the term $a_{-1}^{(n)} W_{-1}(\omega, \mathbf{r}_j; c(\omega))$ in a fit to eq. (10) may be approximated with $A^{(n)} \exp[-ik(\Delta_j^{(n)} - \Delta)]$ for a constant $A^{(n)}$. The constants

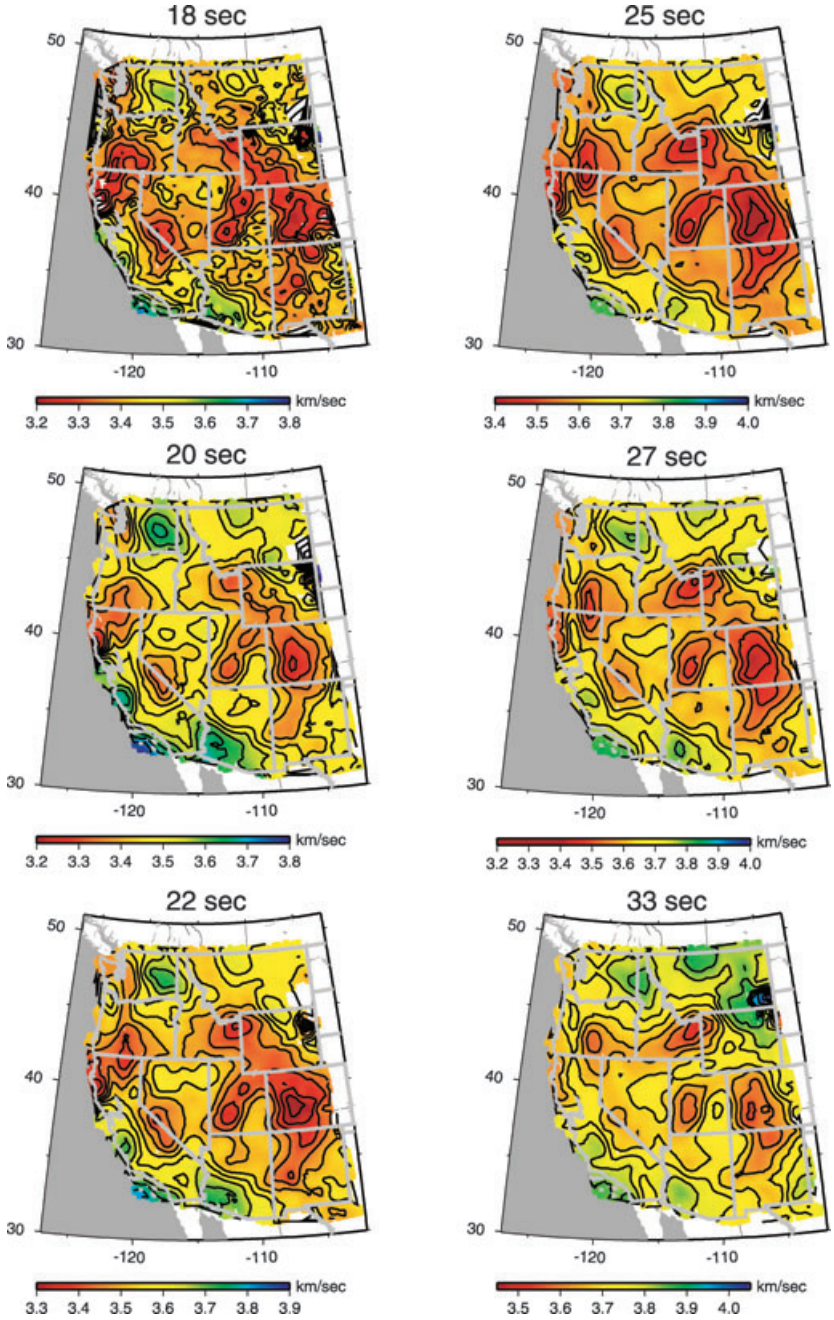

Figure 7. Phase-velocity maps derived using local wavefield fits with the plane-wave term W_{-1} and non-plane-wave terms W_0 and W_1 in eq. (10) [i.e. $l_{\max} = 1$].

$\{A^{(n)}\}$ for all events and wavenumber k are to be determined jointly as described in Section 3. If standard errors σ_j are assigned to the observed wavefield potentials [more precisely, to both the real and imaginary parts of $\tilde{\Phi}^{(n)}(\omega, \mathbf{r}_j)$], then a linearized analysis in terms of unknown variables $A^{(n)}$ and k about their estimated values shows that the variance in estimated wavenumber is

$$\mathrm{var}(k) = \left[\sum_{n=1}^{N} \sum_{j \in \mathrm{Event}\#n} \left(\Delta_j^{(n)} - \Delta \right)^2 \frac{|A^{(n)}|^2}{\sigma_j^2} \exp\left(-\frac{|\mathbf{r}_0 - \mathbf{r}_j|^2}{d^2} \right) \right]^{-1}. \quad (13)$$

The variance in $c = \omega/k$ is then

$$\mathrm{var}(c) = c^2 \frac{\mathrm{var}(k)}{k^2}. \quad (14)$$

We use the residual variance in the plane wave fits as a guide to the ratio $|A^{(n)}|/\sigma_j$. For example, at 50s the residual variance is typically about 4 percent, and we choose $|A^{(n)}|/\sigma_j = 1/\sqrt{(0.02)} \approx 7.1$. (The introduction of this constant ratio is consistent with the solution for c obtained by minimizing the function in eq. 9.) Fig. 8 shows the resulting errors in phase-velocity maps at periods 20, 50 and 100 s.

At longer period, the transition to higher seismic velocity in the eastern part of the study area is consistent with regional studies (e.g. Goes & van der Lee 2002; Marone *et al.* 2007). At all common periods (i.e. $\geq$25 s) our phase-velocity maps are highly correlated with those of Yang *et al.* (2008), which are based on earthquake tomography. At shorter period there is excellent agreement with

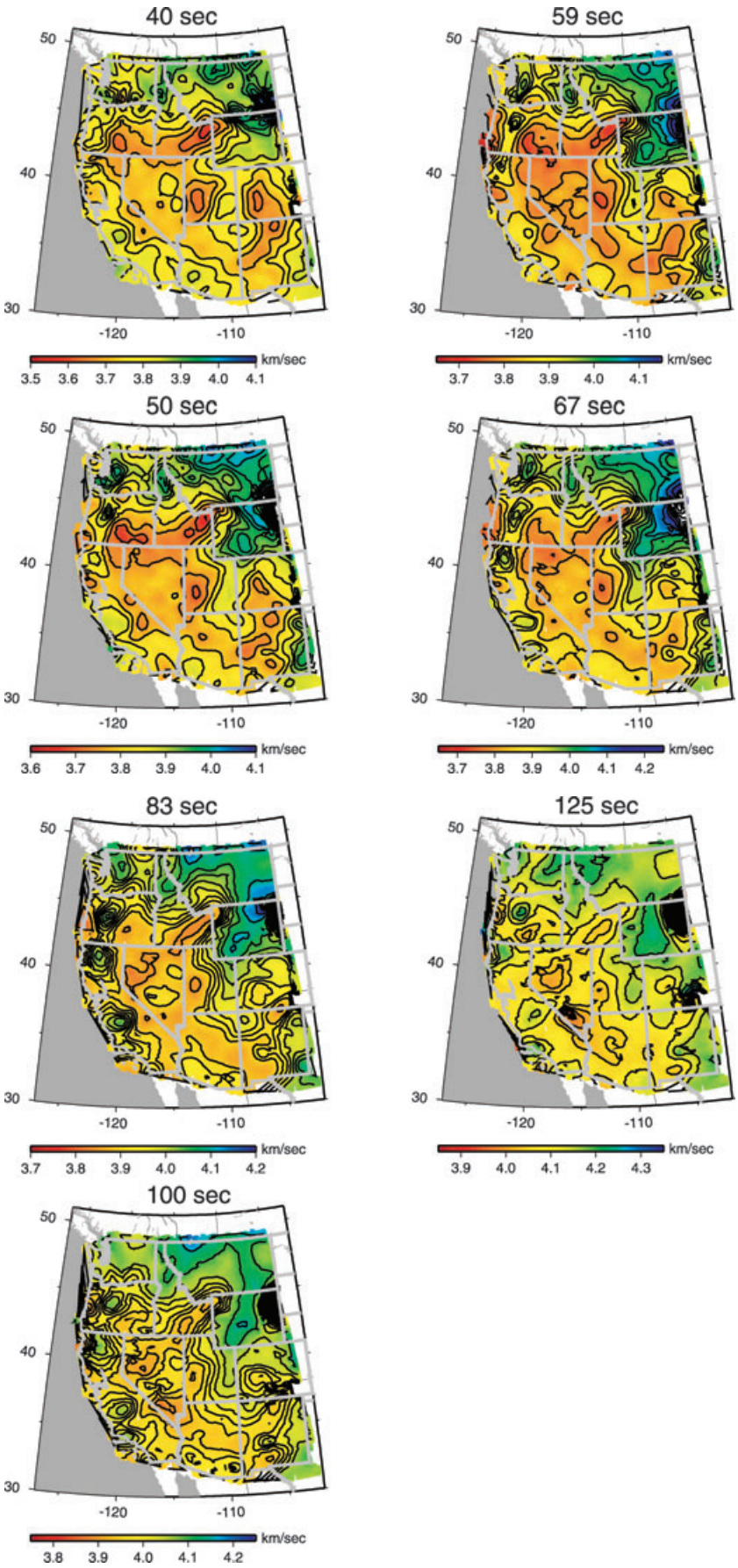

Figure 7. (*Continued.*)

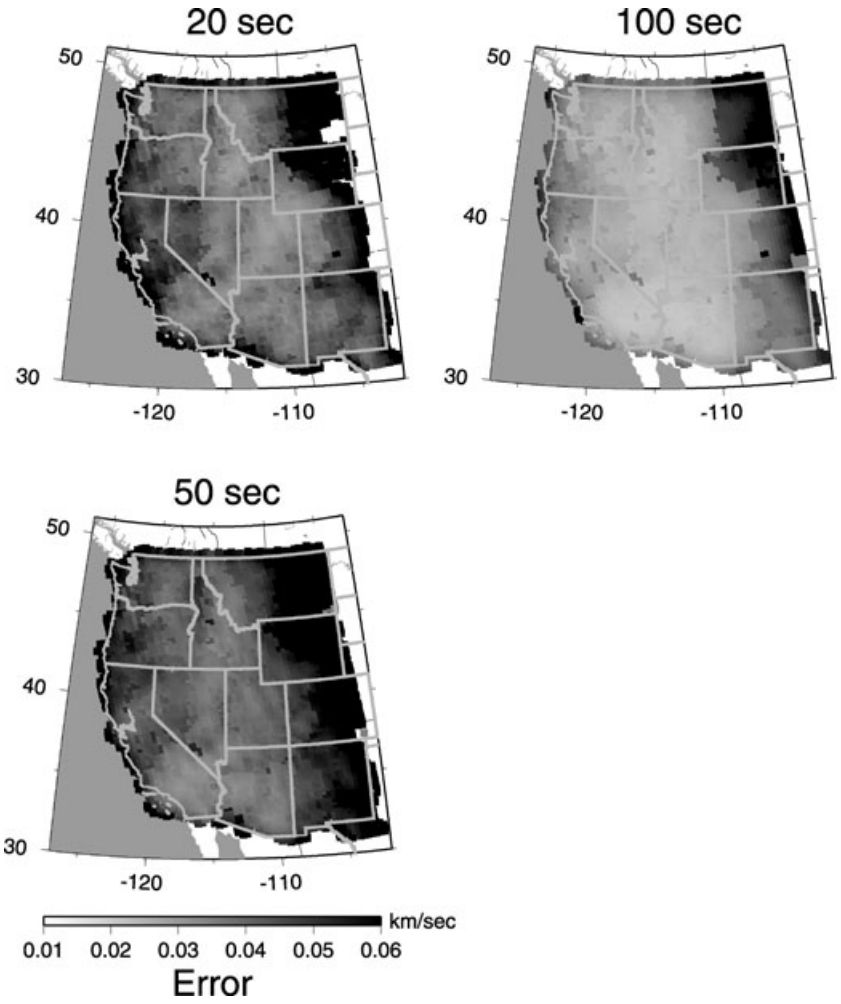

Figure 8. Standard errors in phase-velocity distribution.

the results of ambient noise tomography (Lin *et al.* 2008; Yang & Ritzwoller 2008).

5 DISCUSSION

5.1 Significance of non-plane waves

The a_{-1} term of eq. (10) represents a plane wave and each term in the l-summation represents a superposition of an infinity of plane waves arriving from a continuum of backazimuths, constrained to be close to the source backazimuth; we term those waves in the l-summation to be 'non-plane' waves. Observations indicate that non-plane waves are generally a considerable part of observed surface wavefields (e.g. Friederich *et al.* 1993, 1994; Pollitz 2008). Whether or not to include the non-plane waves in the parameterization of Φ is tantamount to judging whether or not the non-plane contributions to the phase-velocity estimation tend to zero statistically as the number of observations increases. This is suggested by eq. 7 of Wielandt (1993), which shows that plane waves contribute to local wavenumber ('structural wavenumber' in Wielandt's terminology) to the spatial gradient in wavefield phase, whereas the non-plane waves contribute to local wavenumber through spatial gradients in wavefield amplitude. The latter are expected to average out for a large number of wavefields arriving with diverse amplitude patterns, and the former are expected to add coherently with each wavefield.

In Fig. 9, we compare the phase-velocity maps at 20, 50 and 100s resulting from the different limits $l_{\max} = -1$, 0, or 1 in eq. (10). (The case $l_{\max} = -1$ is a single plane wave with only the a_{-1} term of eq. 10.) The inclusion of non-plane waves in the cases $l_{\max} = 0$ or 1 produces minor differences in results at 20 and 50 s relative to the case $l_{\max} = -1$, but it produces marked differences at 100s. This is at first glance surprising because non-plane-wave effects are relatively large at shorter period when judged by the variations in wavefield amplitude across a network (Friederich *et al.* 1993, 1994). However, the amplitude variations are counterbalanced to a large extent by the larger wavenumber at shorter period, which tends to reduce the error in relative phase-velocity distribution according to eqs (13) and (14). Thus at relatively short period, the stabilizing effect of larger wavenumber in the present scheme of estimating lateral wavenumber variations, using a network of fixed aperture, evidently outweighs the destabilizing effect of larger amplitude variations.

A natural question is whether or not the inclusion of non-plane-wave terms in eq. (10) is statistically significant. We address this by modifying our procedure slightly. We choose to perform local fits with only the nearest six seismic stations to the given target point, simultaneously removing the dependence of the misfit function on smoothing distance d (in practice, we assign a very large value to d in this experiment). For a given target point $\mathbf{r}_0$, let $\chi^2(l_{\max})$ denote the global minimum misfit (eq. 10) obtained by fitting a phase velocity value to observations from N sources. (The value

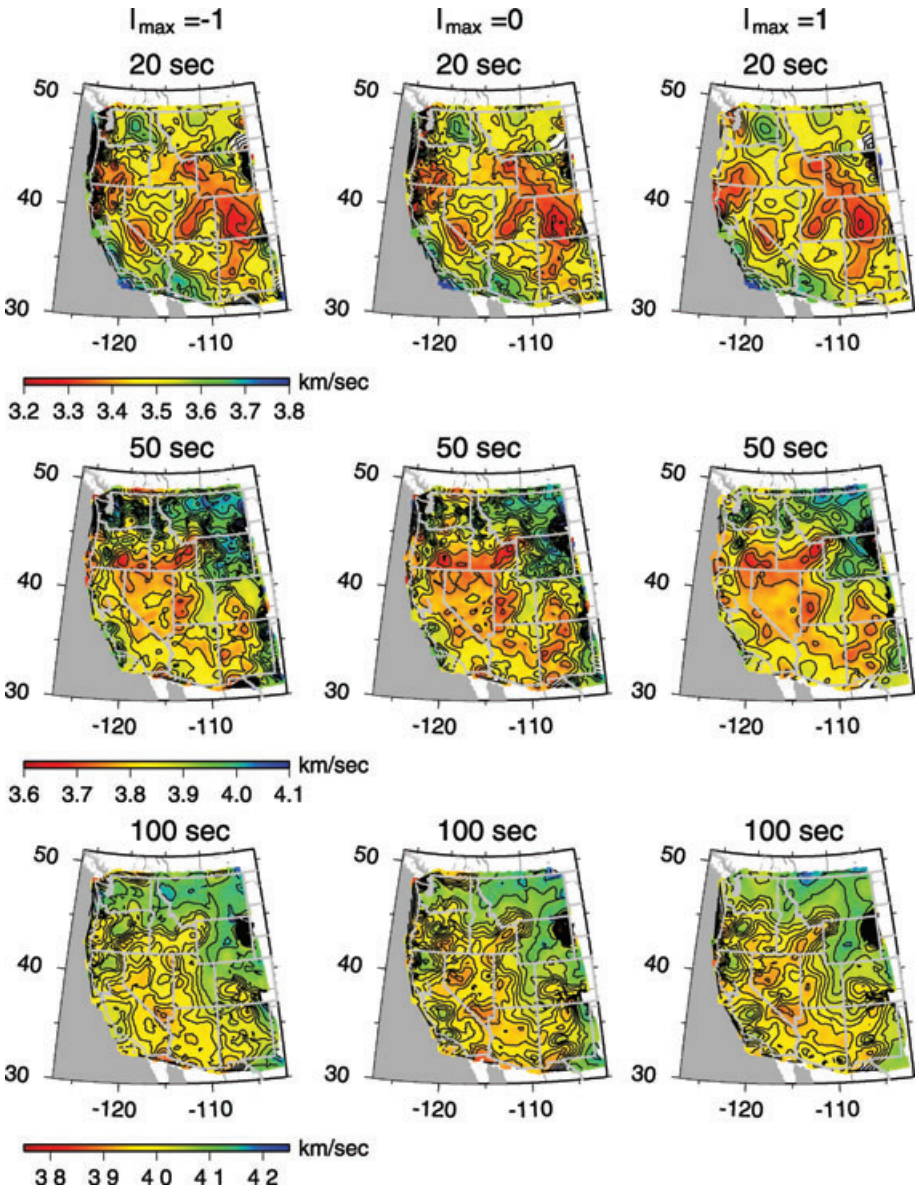

Figure 9. Phase-velocity maps at various periods derived using different values of $l_{\max}$ in eq. (10). The case $l_{\max} = -1$ is the plane wave approximation (only the a_{-1} term used in eq. 10).

of N generally depends on $\mathbf{r}_0$ because different regions have been occupied by TA stations at different times, and we stipulate that for a given source, at least one operating TA station be within 50 km of the target point.) There are $12N$ data and $P = 2N(l_{\max} + 2) + 1$ parameters involved with fitting these data with N sets of waves of the form eq. (10) plus the phase velocity. Hence the function

$$F = \frac{\left[\chi^2(l_{\max}) - \chi^2(l_{\max} + 1)\right]/(2N)}{\chi^2(l_{\max})/(12N - P)} \tag{15}$$

is distributed with $2N$ and $12N - P$ degrees of freedom (e.g. Bevington 1969). An $F-$test yields the significance of the addition of one non-plane wave at every target point. After compiling significance values at all target points, Fig. 10 shows histograms of the significance of successively adding non-plane-wave terms W_0, W_1 and W_2 to the local fits of the wavefields using eq. (10). The first two non-plane terms are highly significant (nearly all significance values greater than 99 percent), but the significance is less pronounced for the W_2 term; the results presented in Fig. 7 are derived from wavefield fits up to the W_1 term.

5.2 Tectonic implications

A 3-D shear velocity model based in the present phase-velocity maps is presented in the Appendix, and it is summarized with depth slices and vertical slices in Fig. 11 and Fig. S1 (parts 1–19, see Supporting Information section), respectively. The 3-D model is available in text form in the Supporting Information.

Many velocity anomalies present in the phase-velocity maps and 3-D model are witnessed in independent results from body wave tomography (e.g. Dueker *et al.* 2001; Burdick *et al.* 2008; Roth *et al.* 2008) and surface wave tomography (e.g. Yang & Ritzwoller 2008; Yang *et al.* 2008; Warren *et al.* 2008). This includes: low velocity anomalies along the Yellowstone–Snake–River Plain (YSRP), High Lava Plains (HLP), Eastern California Shear Zone, the Intermountain Seismic Belt and the Rio Grande Rift (RGR); high velocity

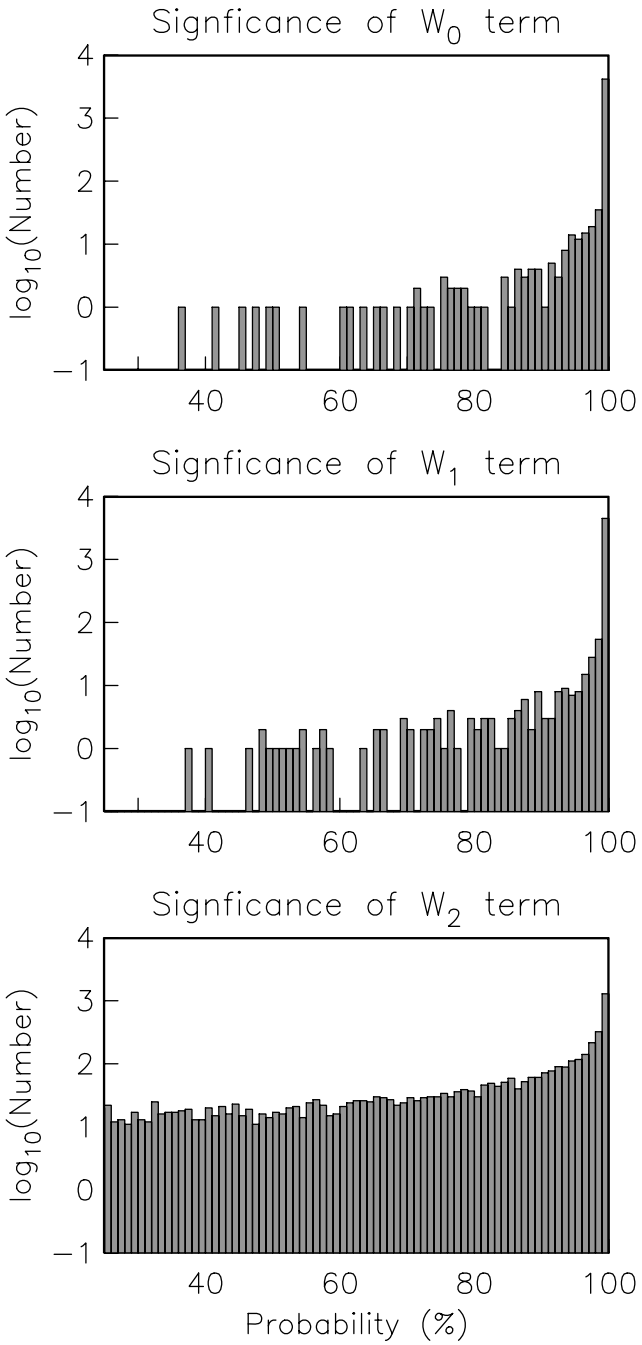

Figure 10. Histograms of the significance of the addition of non-plane-wave terms W_0, W_1 and W_2 when fitting wavefields with eq. (10).

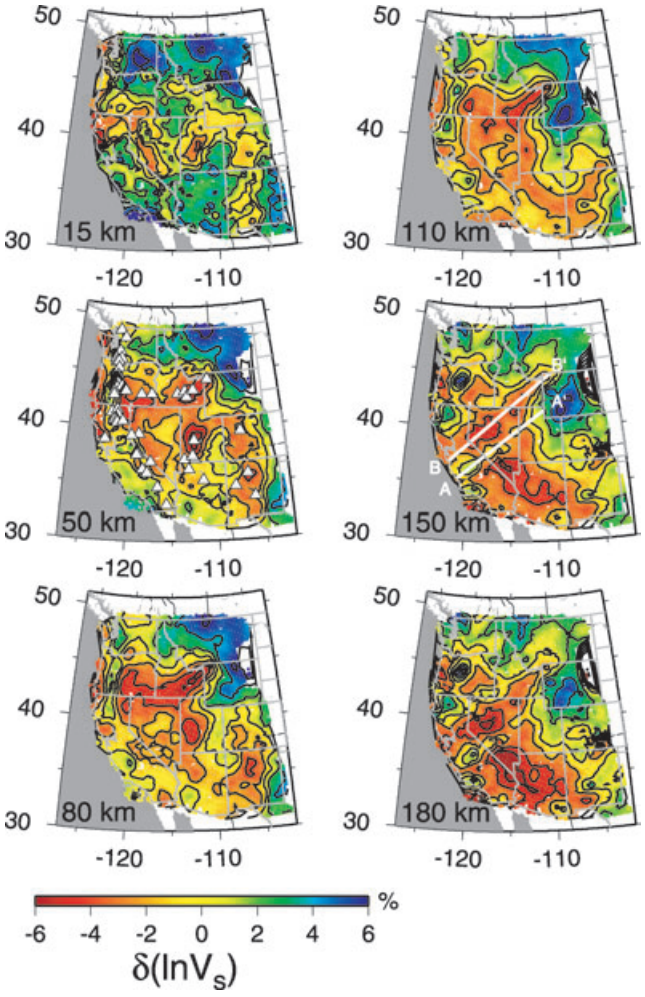

Figure 11. Perturbation in shear velocity with respect to a reference model (Fig. 17 of Pollitz 2008) in map views. Centers of Holocene and Pleistocene volcanism (Siebert & Simkin 2002) are indicated in the 50 km depth slice.

anomalies within the Columbia Plateau, southern Great Valley, the Wyoming craton, Wallowa Mountains and Idaho batholith (both at $\gtrsim$50 s and hence at greater depth), and the narrow region (100–200km wide around longitude 110°W and south of 40°N) dividing the southern Rocky Mountains and Rio Grande Rift from the northern and southern Basin and Range domains.

The 3-D velocity pattern supports previous interpretations based on local tomography in various localities. For example, the patterns of low-velocity uppermost mantle to high-velocity mantle at $\gtrsim$100 km depth around the Wallowa Mountains (Grande Ronde uplift) and $\gtrsim$50 km depth around the southern Sierra Nevada agree with the *P*-wave tomographic images of Hales *et al.* (2005) and Saleeby & Foster (2004). This results support their respective interpretations of mantle delamination based on the seismic velocity patterns and associated uplift. We image low velocity mantle persisting to about 150–200 km depth below the YSRP and the HLP, in agreement with local studies (e.g. Christiansen *et al.* 2002; Yuan & Dueker 2005; Waite *et al.* 2006; Warren *et al.* 2008). Our results confirm the findings of Warren *et al.* (2008) that the low-velocity anomaly of the HLP is slightly weaker than that of the YSRP and that it is concentrated at about 50 km depth in southeast Oregon, where it is correlated with extensive volcanism over the past 25 Myr. In New Mexico, the RGR is expressed as a distinct low-velocity feature in the mantle down to about 110 km depth, in agreement with the surface wave results of Wilson *et al.* (2005). However, the low-velocity mantle follows more closely the trend of the Jemez lineament (Karlstrom 1999) rather than the surface expression of the RGR, suggesting that the location of the RGR may be controlled, at least in paper, by a pre-existing zone of weakness in the shallow mantle; the existence of such a weak zone was also suggested by Wilson *et al.* (2005) based on the difficulty of matching a mechanical model of rifting with the width and amplitude of the observed mantle seismic velocity anomaly. The lineament appears to correspond to a Proterozoic boundary between the Yavapai and Mazatzal provinces

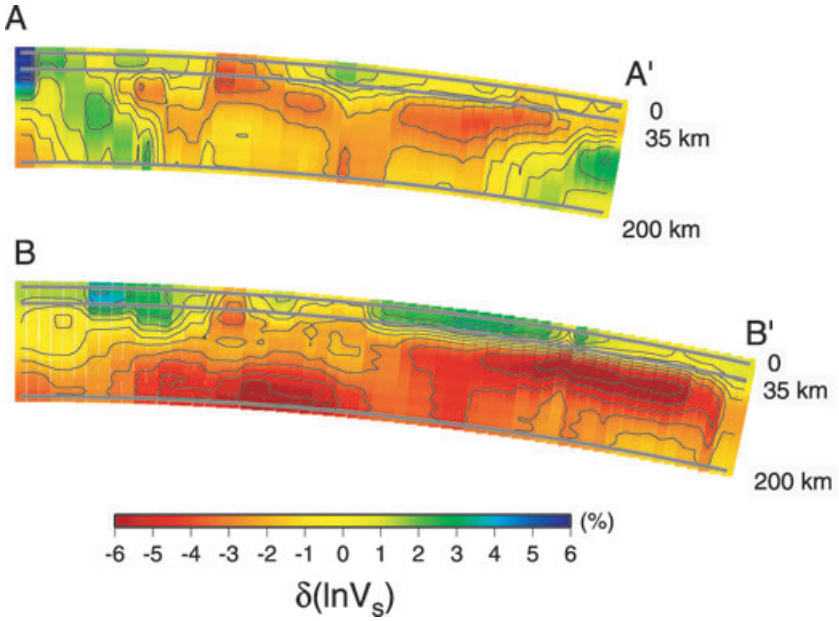

Figure 12. Shear velocity structure along two profiles through the Great Basin (locations in Fig. 11).

(Karlstrom & Humphreys 1998). At depth $\gtrsim$110 km, low-velocity mantle is concentrated south and west of the RGR in a broad area of the southern Great Basin that has undergone relatively large amounts of Cenozoic extension.

The phase-velocity maps from ∼33 to 100 s, as well as corresponding depth slices at depth ∼50–150 km (Fig. 11), are highly correlated with both effective elastic plate thickness (Lowry *et al.* 2000) and heat flow (e.g. Fig. 4 of Dixon *et al.* 2004). This applies to low velocities of the HLP, the Great Basin (excluding central Nevada), the RGR and Colorado Plateau, which correlate with low elastic plate thickness and high heat flow, and to high velocities of the 110°W lineament, the Juan de Fuca slab, and central Nevada, which correlate with high elastic plate thickness and low heat flow. Notwithstanding exceptional regions where these correlations are weaker (e.g. southern Sierra Nevada, Snake River Plain), this suggests that temperature plays the dominant role in shaping mantle seismic velocities at least from ∼50 to 150 km depth. It is also noteworthy that low-velocity regions in the 50-km depth slice correlate with the distribution of Holocene and Pleistocene volcanoes (Fig. 11), and that these anomalies also correlate with crustal seismicity, for example in the HLP, Walter Lane and Eastern California Shear Zone and Intermountain Seismic Belt. This suggests that hot mantle around ∼50 km depth in these regions provides the heat source for associated magmatism as well as thinning of the thermal lithosphere, leading to relatively high stress concentration.

At depth $\gtrsim$100 km, there emerges a SW–NE trending relatively high-velocity lineament from the southern Great Valley anomaly (SGVA; 36°N, 119°W) through central Nevada and northern Utah (Fig. 12). The portion of the anomaly in south-central Nevada—within the middle of this corridor—coincides with a high velocity anomaly imaged by West *et al.* (2009) to great depth (∼800 km). West *et al.* (2009) propose that the shallower expression of the anomaly represents a mantle delamination but also suggest that it merges with fossil slab at depth greater than about 500 km. Given the depth of the anomaly $\gtrsim$100 km (Fig. 11), we suggest that this feature may be a relic of subduction, perhaps in the manner proposed by Humphreys (1995), or, alternatively, a deep remnant of the Mojave Province (Karlstrom & Humphreys 1998).

Adjacent to the imaged SGVA to northern Utah and 110°W high-velocity lineaments are three bordering low-velocity (presumably high temperature) domains pointed out by Karlstrom (1999), one along the Jemez lineament through New Mexico and Arizona, one running along the St. Georges lineament through central Utah and the third along the Snake River Plain. In this context, the imaged high-velocity lineaments define the boundaries of the high-temperature domains more precisely.

High velocity anomalies associated with the subducting Juan de Fuca slab are clearly present at period $\geq$25 s and locate progressively eastward with increasing period. The phase-velocity maps at longer period suggest that the slab signal is weak in southern Oregon, where continuity with the slab signal to its north and south is tenuous.

6 CONCLUSIONS

Using two and three-quarter years of data from the Transportable Array, we use local tomography based on the spherical Helmholtz equation to image fundamental-mode Rayleigh-wave phase-velocity structure from 18 to 125 s period. We use the Transportable Array as essentially a large number of smaller arrays. By treating every local wavefield as non-plane wavefield, the methodology accounts for surface wave scattering over the surrounding region without needing to invoke the solution of an integral equation or solve for incident wavefields over a large domain. Although applied here to a large network, the method is also naturally applicable to a smaller regional network as long as the station spacing is of the same order as the scale length used to localize the phase-velocity fits (eq. 12).

The non-plane components of the wavefield are statistically significant, supporting the interpretation—based on the spherical Helmholz equation—that local observations are systematically shaped by remotely generated scattering interactions. A trade-off remains between inferred phase-velocity structure and the form of the non-plane wavefields used to estimate the local wavefields, that is the cut-off $l_{\max}$ in eq. (10). This trade-off is significant at

progressively longer period because the aperture of each subset of the TA used in the local fits of eq. (9) tends to a smaller number of wavelengths with increasing period.

The phase-velocity maps of Fig. 7 update the maps presented by Pollitz (2008), which are based on about one-third the data and cover roughly the western half of this study area. These maps are similar but reveal more detail than the Pollitz (2008) maps, particularly at longer period. We attribute this to not only the greater amount of data but also the robustness of this method. The former method involves fitting each observed wavefield with an incident non-plane wavefield jointly with solving an integral equation for phase-velocity structure; a large number of unknowns are involved in both steps, and multiple scattering is required to synthesize the wavefield accurately at successively greater propagation distance from the source. This approach involves only local fits of non-plane wavefields with relatively few parameters and is therefore more robust. Moreover, it is consistent with the scattering theory (eq. 6) that forms the basis of the former method.

The phase-velocity maps are suitable for constraining depth-dependent seismic velocity within the upper ∼200 km (Appendix A). In a follow-up study, we anticipate combining the phase-velocity maps with body wave traveltimes in a joint surface wave/body wave tomography study.

ACKNOWLEDGMENTS

Source locations and magnitudes are from the NEIC catalogue. Data from the Transportable Array was provided by the Incorporated Research Institutions for Seismology (IRIS) Data Management Center. This manuscript benefitted from reviews by Barbara Romanowicz and Derek Schutt and Associate Editor Gabi Laske. We are grateful to several colleagues for their suggestions on improving the study, particularly to David James and Walter Mooney for engaging discussions and David Hill, John Evans and Bill Ellsworth for their comments on a preliminary draft.

REFERENCES

Abramowitz, M. & Stegun, I., 1972. *Handbook of Mathematical Functions*, Vol. 1, U.S. Department of Commerce, National Bureau of Standards, Washington, DC.

Alsina, D., Woodward, R.L. & Snieder, R., 1996. Shear wave velocity structure in North America from large-scale waveform inversions of surface waves, *J. geophys. Res.,* **101,** 15 969–15 986.

Bevington, P.R., 1969. *Data Reduction and Error Analysis for the Physical Sciences,* McGraw-Hill, New York.

Burdick, S. et al., 2008. Upper-mantle heterogeneity beneath North America from Travel Time Tomography with Global and USArray Data, *Seism. Res. Lett.,* **79,** 384–392.

Cara, M., 1978. Regional variations of higher Rayleigh-mode phase velocities: a spatial filtering method, *Geophys. J. R. astr. Soc.,* **54,** 439–460.

Christiansen, R.L., Foulger, G.R. & Evans, J.R., 2002. Upper-mantle origin of the Yellowstone hotspot, *GSA Bull.,* **114,** 1245–1256.

Chulick, G.S. & Mooney, W.D., 2002. Seismic Structure of the Crust and Uppermost Mantle of North America and adjacent oceanic basins: a synthesis, *Bull. seism. Soc. Am.,* **92,** 2478–2492.

Dahlen, F.A. & Tromp, J., 1998. *Theoretical Global Seismology,* Princeton University Press, Princeton, NJ.

Dixon, J.E., Dixon, T.H., Bell, D.R. & Malservisi, R., 2004. Lateral variation in upper mantle viscosity: role of water, *Earth planet. Sci. Lett.,* **222,** 451–467.

Dueker, K., Yuan, H. & Zurek, B., 2001. Thick-structured Proterozoic lithosphere of the Rocky Mountain region, *GSA Today,* **11,** 4–9.

Dziewonski, A. & Anderson, D., 1981. Preliminary reference earth model, *Phys. Earth planet. Inter.,* **25,** 297–356.

Dziewonski, A.M., Block, S. & Landisman, M., 1969. A technique for analysis of transient seismic signals, *Bull. seism. Soc. Am.,* **59,** 427–444.

Forsyth, D.W. & Li, A., 2005. Array-analysis of two-dimensional variations in surface wave phase velocity and azimuthal anisotropy in the presence of multipathing interference, in *AGU Geophysical Monograph 187,* pp.81–98, eds Levander, A. & Nolet, G., Washington, DC.

Forsyth, D.W., Webb, S.C., Dorman, L.M. & Shen, Y., 1998. Phase velocities of Rayleigh waves in the MELT Experiment on the East Pacific Rise, *Science,* **22,** 1235–1238.

Friederich, W., 1998. Wave-theoretical inversion of teleseismic surface waves in a regional network: phase velocity maps and a three-dimensional upper-mantle shear wave velocity model for southern Germany, *Geophys. J. Int.,* **132,** 203–225.

Friederich, W., 1999. Propagation of seismic shear and surface waves in a laterally heterogeneous mantle by multiple forward scattering, *Geophys. J. Int.,* **136,** 180–204.

Friederich, W. & Wielandt, E., 1995. Interpretation of seismic surface waves in regional networks: joint estimation of wavefield geometry and local phase velocity method and numerical tests, *Geophys. J. Int.,* **120,** 731–744.

Friederich, W., Stange, S. & Wielandt, E., 1993. Multiple forward scattering of surface waves: comparison with exact solution and Born scattering methods, *Geophys. J. Int.,* **112,** 264–275.

Friederich, W., Wielandt, E. & Stange, S., 1994. Non-plane geometries of seismic surface wavefields and their implications for regional-scale surface-wave tomography, *Geophys. J. Int.,* **119,** 931–948.

Friederich, W., Hunzinger, S. & Wielandt, E., 2000. A note on the interpretation of seismic surface waves over three-dimensional structures, *Geophys. J. Int.,* **143,** 335–339.

Goes, S. & van der Lee, S., 2002. Thermal structure of the North American uppermost mantle inferred from seismic tomography, *J. geophys. Res.,* **107,** 10.1029/200JB000049.

Goes, S., Govers, R. & Vacher, P., 2000. Shallow mantle temperatures under Europe from P and S wave tomography, *J.geophys. Res.,* **105,** 11 153–11 169.

Hales, T.C., Abt, D.L., Humphreys, E.D. & Roering, J.J., 2005. A lithospheric instability origin for Columbia River flood basalts and Wallowa Mountains uplift in northeast Oregon, *Nature,* **438,** 842–845.

Humphreys, E., 1995. Post-Laramide removal of the Farallon slab, western United States, *Geology,* **23,** 987–990.

Humphreys, E. & Dueker, K., 1994. Western US upper mantle structure, *J.geophys. Res.,* **99,** 9615–9634.

Karlstrom, K.E., 1999. Introduction to the special issues, Paper II: Nature of tectonic boundaries in lithosphere of the Rocky Mountains, *Rocky Mountain Geol.,* **34,** 1–4.

Karlstrom, K.E. & Humphreys, E.D., 1998. Persistent influence of Proterozoic accretionary boundaries in the tectonic evolution of southwestern North America: interaction of cratonic grain and mantle modification events, *Rocky Mountain Geol.,* **33,** 161–179.

Lawson, C.L. & Hanson, R.J., 1974. *Solving Least Squares Problems,* Prentice Hall, Englewood Cliffs, NJ.

Levshin, A.L., Yanovskaia, T.B., Lander, A.V., Bukchin, B.G., Barmin, M.P. & Ramikova, L.I., 1989. Surface waves in vertically inhomogeneous media, in *Surface Waves in a Laterally Inhomogeneous Earth,* pp. 131–182, ed. Keilis-Borok, V.I., Kluwer, Dordrecht.

Lin, F.C., Moschetti, M. & Ritzwoller, M., 2008. Surface wave tomography of the western United States from ambient seismic noise: Rayleigh and Love wave phase velocity maps, *Geophys. J. Int.,* **173,** 281–298.

Lin, F.C., Ritzwoller, M.H. & Snieder, R., 2009. Eikonal tomography: surface wave tomography by phase front tracking across a regional broadband array, *Geophys. J. Int.,* **177,** 1091–1110.

Lowry, A.R., Ribe, N.M. & Smith, R.B., 2000. Dynamic elevation of the Cordillera, western United States, *J. geophys. Res.,* **105,** 23371–23390.

Marone, F., Gung, Y. & Romanowicz, B., 2007. 3d radial anisotropic structure of the North American upper mantle from inversion of surface waveform data, *Geophys. J. Int.,* **171,** 206–222.
Nolet, G. & Dahlen, F.A., 2000. Wavefront healing and the evolution of seismic delay times, *J. geophys. Res.,* **105,** 19 043–19 054.
Nyman, D.C. & Landisman, M., 1977. The display-equalized filter for frequency-time analysis, *Bull. seism. Soc. Am.,* **67,** 393–404.
Park, J., Lindberg, C.R. & Thomson, D.J., 1987. Multiple taper spectral analysis of terrestrial free oscillations: Paper 1, *Geophys. J. R. astr. Soc.,* **91,** 755–794.
Pollitz, F., 2008. Observations and interpretation of fundamental-mode Rayleigh wavefields recorded by the Transportable Array (USArray), *J. geophys. Res.,* **113,** B10311, doi:10.1029/2007JB005556.
Pollitz, F.F., 1999. Regional velocity structure in northern California from inversion of scattered seismic surface waves, *J. geophys. Res.,* **104,** 15 043–15 072.
Romanowicz, B., 1987. Multiplet–multiplet coupling due to lateral heterogeneity: asymptotic effects on the amplitude and frequency of the Earth's normal modes, *Geophys. J. R. astr. Soc.,* **90,** 75–100.
Roth, J.B., Fouch, M.J., James, D.E. & Carlson, R.W., 2008. Three-dimensional seismic velocity structure of the northwestern United States, *Geophys. Res. Lett.,* **35,** L15304, doi:10.1029/2008GL034669.
Saleeby, J.B. & Foster, Z., 2004. Topographic response of mantle lithosphere removal in the southern Sierra Nevada region, *Geology,* **32,** 245–248.
Siebert, L. & Simkin, T., 2002. Volcanoes of the World: An Illustrated Catalog of Holocene Volcanoes and their Eruptions, *Volcanism Program Digital Information Series,* vol. GVP-3, Smithsonian Institution.
Sigloch, K., McQuarrie, N. & Nolet, G., 2008. Two-stage subduction history under North America inferred from multiple-frequency tomography, *Nature Geosci.,* **1,** 458–462.
Smith, M.L. & Dahlen, F.A., 1973. Azimuthal dependence of Love and Rayleigh-wave propagation in a slightly anisotropic medium, *J. geophys. Res.,* **78,** 3321–3333.
Snieder, R., 1986. 3-D linearized scattering of surface waves and a formalism for surface wave holography, *Geophys. J. R. astr. Soc.,* **84,** 581–605.
Tromp, J. & Dahlen, F.A., 1993. Variational principles for surface wave propagation on a laterally heterogeneous Earth—III: potential representation, *Geophys. J. Int.,* **112,** 195–209.
Waite, G.P., Smith, R.B. & Allen, R.M., 2006. Vp and Vs structure of the Yellowstone hotspot from teleseismic tomography: evidence for an upper-mantle plume, *J. geophys. Res.,* **111,** B04303, doi:10.1029/2005JB003867.
Wang, Z. & Dahlen, F.A., 1995. Validity of surface-wave ray theory on a laterally heterogeneous Earth, *Geophys. J. Int.,* **123,** 757–773.
Warren, L.M., Snoke, J.A. & James, D.E., 2008. S-wave velocity structure beneath the High Lava Plains, Oregon, from Rayleigh-wave dispersion inversion, *Earth planet. Sci. Lett.,* **274,** 121–131.
West, J.D., Fouch, M.J., Roth, J.B. & Elkins-Tanton, L.T., 2009. Vertical mantle flow associated with a lithospheric drip beneath the Great Basin, *Nature Geosci.,* **2,** 439–444.
Wielandt, E., 1993. Propagation and structural interpretation of non-plane waves, *Geophys. J. Int.,* **113,** 45–53.
Wielandt, E. & Schenk, H., 1983. On Systematic Errors in Phase-Velocity Analysis, *J. Geophys.,* **52,** 1–6.
Wilson, D. et al., 2005. Lithospheric structure of the Rio Grande Rift, *Nature,* **433,** 851–855.
Yang, Y. & Forsyth, D.W., 2006. Rayleigh wave phase velocities, small-scale convection, and azimuthal anisotropy beneath southern California, *J. geophys. Res.,* **111,** doi:10.1029/2005JB004180.
Yang, Y. & Ritzwoller, M.H., 2008. Teleseismic surface wave tomography in the western US using the Transportable Array component of USArray, *Geophys. Res. Lett.,* **35,** L04308, doi:10.1029/2007GL032278.
Yang, Y., Ritzwoller, M.H., Lin, F.C., Moschetti, M.P. & Shapiro, N.M., 2008. Structure of the crust and uppermost mantle beneath the western United States revealed by ambient noise and earthquake tomography, *J.geophys. Res.,* **113,** B12310, doi:10.1029/2008JB005833.
Yuan, H. & Dueker, K., 2005. Teleseismic P-wave tomogram of the Yellowstone plume, *Geophys. Res. Lett.,* **32,** L07304, doi:10.1029/2004GL022056.
Zhou, Y., Dahlen, F.A. & Nolet, G., 2004. Three-dimensional sensitivity kernels for surface wave observables, *Geophys. J. Int.,* **158,** 142–168.

APPENDIX A: THREE-DIMENSIONAL SHEAR VELOCITY STRUCTURE

This appendix describes how 3-D shear velocity structure in the upper 200 km of the western United States is derived from the surface wave phase-velocity maps (Fig. 7). The 3-D model is presented as both depth slices and vertical cross-sections.

At each of approximately 6000 target points (number depending on period) spanning the Transportable Array (Fig. 1), we have available values of frequency-dependent phase velocity $c(\mathbf{r}, f)$ at 13 periods $T = 1/f_i$ ranging from 18 to 125 s. We use the following steps to derive 3-D structure.

(1) Correct $c(\mathbf{r}, f)$ for the effect of lateral variations in crustal thickness. For this purpose we use a smoothed map of these variations derived from a North American database (Fig. A1). For each $\mathbf{r}$ and f, we take a reference laterally homogeneous model (Fig. 17 of Pollitz (2008), which is the PREM model with a 35 km thick continental crust and a reduced velocity of 3 percent from 35 to 220 km) and adjust the crustal thickness from the reference value of $h_0 = 35$ km to the crustal thickness at $\mathbf{r}$. Denoting the phase velocity on the laterally heterogeneous model with crustal thickness $h(\mathbf{r})$ as $c_0(h(\mathbf{r}), f)$, the corrected phase velocities are

$$c_{\rm corr}(\mathbf{r}, f) = c(\mathbf{r}, f) - c_0(h(\mathbf{r}), f) + c_0(h_0, f). \quad \text{(A1)}$$

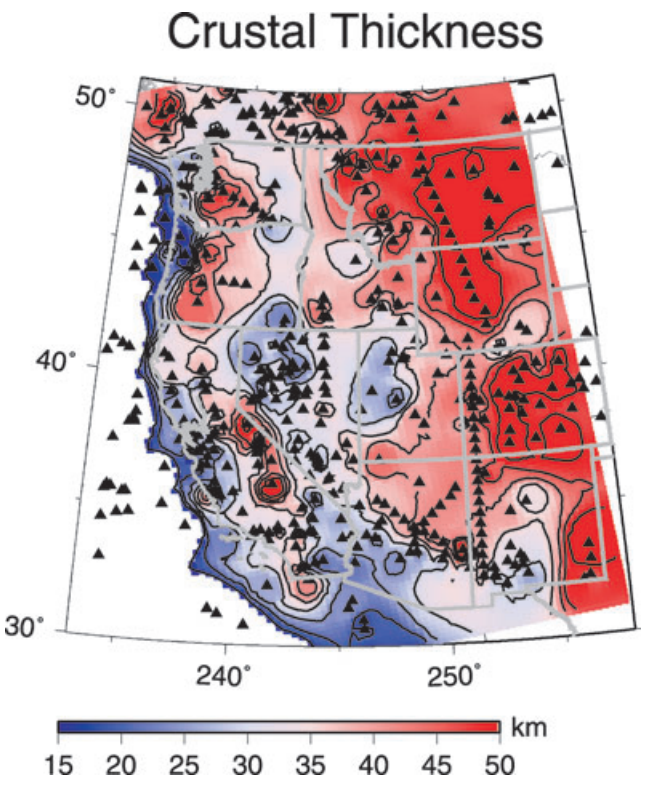

Figure A1. Smoothed crustal thickness over the western United States derived from the North American database of Chulick & Mooney (2002). Locations of crustal thickness estimates in that database are indicated with triangles.

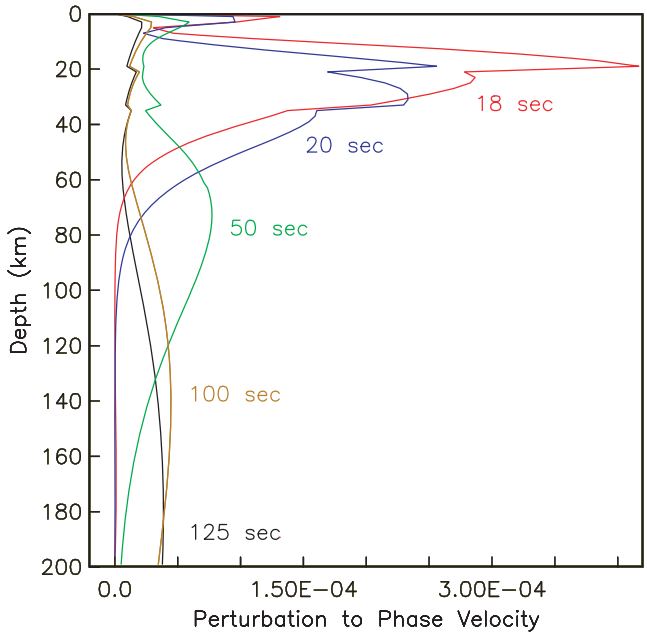

Figure A2. Frechét kernels for phase velocity at various periods. The reference model is the WUS reference model of Fig. 17 of Pollitz (2008) with a 35 km crustal thickness.

(2) Derive local Frechét kernels $K(r, f)$ which yield the sensitivity of local isotropic phase velocity to a perturbation in shear velocity at radius r. From eqs (83) and (I.6) of Romanowicz (1987), phase velocity is related to perturbations in structural parameters as

$$\frac{\delta c(\mathbf{r}, f)}{c_0(h_0, f)} = \frac{c_0}{\omega U} \int_0^R \Big[\delta\mu(r, \mathbf{r}) M_{1K}^{(0)}(r) + \delta\kappa(r, \mathbf{r}) M_{2K}^{(0)}(r) + \delta\rho(r, \mathbf{r}) M_{3K}^{(0)}(r)\Big] r^2 \, dr \tag{A2}$$

where $\omega = 2\pi f$; U is group velocity; $\delta\mu$, $\delta\kappa$ and $\delta\rho$ are perturbations in shear modulus, bulk modulus and density, respectively; the $M_{jK}^{(0)}$ are defined in Table 1 of Romanowicz (1987). The integration is taken over radius up to Earth's radius R. Using scaling relations among seismic velocities and density assuming a thermal origin (Humphreys & Dueker 1994; Goes *et al.* 2000):

$$\frac{\delta \ln \rho}{\delta \ln v_p} = 0.4, \quad \frac{\delta \ln v_s}{\delta \ln v_p} = 1.7, \tag{A3}$$

we may write eq. (A2) in the form

$$\frac{\delta c(\mathbf{r}, f)}{c_0(h_0, f)} = \int_0^R \frac{\delta v_s(r, \mathbf{r})}{v_s(r, \mathbf{r})} K(r, f) \, dr \tag{A4}$$

where v_s is shear velocity. Again using the reference laterally homogeneous model shown in Fig. 17 of Pollitz (2008), examples of $K(r, f)$ at various periods are shown in Fig. A2.

(3) At every target point $\mathbf{r}$, perform a separate inversion for shear velocity by minimizing

$$\chi^2(\mathbf{r}) = \sum_{i=1}^{13} \left[\frac{\delta c(\mathbf{r}, f_i)}{c_0(h_0, f_i)} - \int_0^R \frac{\delta v_s(r, \mathbf{r})}{v_s(r, \mathbf{r})} K(r, f_i) \, dr \right]^2 \frac{1}{\sigma_i^2(\mathbf{r})} \tag{A5}$$

where $\sigma_i(\mathbf{r})$ is the standard error in the phase-velocity distribution at frequency f_i and

$$\delta c(\mathbf{r}, f_i) = c_{\text{corr}}(\mathbf{r}, f_i) - c_0(h_0, f_i). \tag{A6}$$

For each $\mathbf{r}$, δv_s is parameterized using 23 Hermite polynomials as a function of depth, and $\chi^2(\mathbf{r})$ is minimized subject to a smoothness constraint on δv_s, yielding the weighting coefficients of the Hermite polynomials. This procedure is repeated at all target points independently.

The resulting shear velocity in the western United States is shown in Fig. 11 in depth slices and Fig. S1 (parts 1–19, see Supporting Information) in a series of vertical cross-sections.

SUPPORTING INFORMATION

Additional Supporting Information may be found in the online version of this article:

Fig. S1. Smoothed crustal thickness over the western US derived from the North American database of Chulick & Mooney (2002). Locations of crustal thickness estimates in that database are indicated with triangles.

Fig. S2. Frechet kernels for phase velocity at various periods. The reference model is the WUS reference model of fig. 17 of Pollitz (2008) with a 35-km crustal thickness.

Fig. S3. Perturbation in shear velocity with respect to the WUS reference model (fig. 17 of Pollitz 2008) invertical cross-sections. Notable tectonic features and/or interpretations are annotated.

Please note: Wiley-Blackwell are not responsible for the content or functionality of any supporting materials supplied by the authors. Any queries (other than missing material) should be directed to the corresponding author for the article.